



Cite this: *Analyst*, 2024, **149**, 5184

# Revealing the heterogeneous catalytic kinetics of PtRu nanocatalysts at the single particle level†

Bowe Zhang,<sup>a,b</sup> Dezheng Zhang,<sup>a,b</sup> Jinpeng Bao,<sup>a</sup> Ce Han,<sup>a</sup>  <sup>✉</sup> Ping Song<sup>\*a</sup> and Weilin Xu  <sup>✉,a,b</sup>

Comparison of the structural features and catalytic performance of bimetallic nanocatalysts will help to develop a unified understanding of structure–reaction relationships. The single-molecule fluorescence technique was utilized to reveal the differences in catalytic kinetics among PtRu bimetallic nanocatalysts and Pt and Ru monometallic nanocatalysts at the single particle level. The results show that bimetallic nanocatalysts have higher apparent rate constants and desorption rate constants relative to monometallic nanocatalysts, which leads to their higher catalytic activity. At the single particle level, bimetallic nanocatalysts have a wider distribution of apparent rate constants, suggesting that bimetallic nanocatalysts have higher activity heterogeneity relative to monometallic nanocatalysts. By investigating the relationship between the reaction rate and the rate of dynamic activity fluctuations, it was found that spontaneous surface restructuring and reaction-induced surface restructuring of nanoparticles occurred. The surface of bimetallic nanoparticles restructured faster, which made the bimetallic nanocatalysts more active. These findings provide new insights into the design of highly active bimetallic nanocatalysts.

Received 25th July 2024,  
Accepted 2nd September 2024

DOI: 10.1039/d4an01017e

rsc.li/analyst

## Introduction

Bimetallic nanocatalysts are an important class of nanocatalysts in heterogeneous catalysis and show a variety of functionalities and outstanding catalytic activity compared to monometallic nanocatalysts.<sup>1–4</sup> Despite extensive efforts in studying the mechanisms of bimetallic nanocatalysts, the reason for the better performance of bimetallic nanocatalysts compared with their corresponding monometallic counterparts remains unclear.<sup>5–8</sup> PtRu bimetallic nanocatalysts are an important class of alloy materials with excellent catalytic properties in many fields.<sup>9–13</sup>

However, most of the research on PtRu bimetallic nanocatalysts has focused on the ensemble level, where the average information is obtained from the simultaneous measurement of a large number of nanocatalysts.<sup>14–18</sup> Adjusting the ratio of the metal elements for bimetallic nanocatalysts is an important method for tuning their catalytic activity. These nanocatalysts are highly heterogeneous, so the unique properties of individual nanoparticles are hidden from ensemble-averaged measurement.<sup>19–22</sup> Therefore, in order to study the relationship between the activity of PtRu bimetallic nanocatalysts and composition, it is necessary to study the behavior of individual nanoparticles in catalysis. In the last decade, the single-molecule fluorescence technique (SMFT), with the ability to study the catalytic behavior of individual nanocatalysts at the single particle level, has become an important approach in catalysis.<sup>23–27</sup> This technique provides new insights into the catalytic activity and enhances the understanding of nanocatalysis.<sup>28–32</sup> SMFT is widely applied in the characterization of catalytic processes, such as the difference in behaviour between AuAg bimetallic nanocatalysts and Ag nanocatalysts in catalytic processes, and the visualisation of bimetallic activity enhancement on heteronuclear PdAu nanocatalysts at the single particle level.<sup>33,34</sup> To the best of our knowledge, the study of PtRu bimetallic nanocatalysts has not been performed previously using the SMFT.

In this work, we synthesized PtRu bimetallic nanocatalysts with three different ratios, and compared them with monometallic Pt and Ru nanocatalysts as five control groups. The kinetic parameters of the five control groups were obtained by the SMFT using the hydrogen reduction of resazurin to the fluorescent product resorufin as a reaction model. By tracking their catalytic behaviors at the single particle level, we divided the catalytic process into product formation and desorption stages. The kinetic parameters of bimetallic and monometallic

lysts are highly heterogeneous, so the unique properties of individual nanoparticles are hidden from ensemble-averaged measurement.<sup>19–22</sup> Therefore, in order to study the relationship between the activity of PtRu bimetallic nanocatalysts and composition, it is necessary to study the behavior of individual nanoparticles in catalysis. In the last decade, the single-molecule fluorescence technique (SMFT), with the ability to study the catalytic behavior of individual nanocatalysts at the single particle level, has become an important approach in catalysis.<sup>23–27</sup> This technique provides new insights into the catalytic activity and enhances the understanding of nanocatalysis.<sup>28–32</sup> SMFT is widely applied in the characterization of catalytic processes, such as the difference in behaviour between AuAg bimetallic nanocatalysts and Ag nanocatalysts in catalytic processes, and the visualisation of bimetallic activity enhancement on heteronuclear PdAu nanocatalysts at the single particle level.<sup>33,34</sup> To the best of our knowledge, the study of PtRu bimetallic nanocatalysts has not been performed previously using the SMFT.

<sup>a</sup>State Key Laboratory of Electroanalytical Chemistry, Jilin Provincial Key Laboratory of Low Carbon Chemical Power, Changchun Institute of Applied Chemistry, Chinese Academy of Sciences, Changchun 130022, China

<sup>b</sup>School of Applied Chemistry and Engineering, University of Science and Technology of China, Hefei 230026, China. E-mail: hance@ciac.ac.cn, songping@ciac.ac.cn, weilinxu@ciac.ac.cn

†Electronic supplementary information (ESI) available: Experimental details; characterization and single-molecule kinetic equations. See DOI: <https://doi.org/10.1039/d4an01017e>



catalysts showed that the catalytic mechanisms all follow competitive adsorption. Moreover, it is demonstrated that bimetallic catalysts exhibit better performance compared to monometallic catalysts at the single particle level. These results further deepen the understanding of PtRu bimetallic and monometallic catalysts.

## Results and discussion

The PtRu bimetallic nanocatalysts were synthesized by the contemporaneous reduction of  $\text{RuCl}_3$  and  $\text{H}_2\text{PtCl}_6$  with  $\text{NaBH}_4$  as the reducing agent and citric acid as the capping agent.<sup>35</sup> Pt and Ru monometallic nanocatalysts were synthesized using the same method with only one metal precursor. Detailed synthesis information is available in the (ESI†). The quantitative measurement results conducted by inductively coupled plasma atomic emission spectroscopy (ICP-AES) revealed that the components are  $\text{Pt}_{66}\text{Ru}_{34}$ ,  $\text{Pt}_{76}\text{Ru}_{24}$  and  $\text{Pt}_{39}\text{Ru}_{61}$  for PtRu bimetallic nanocatalysts, respectively. Typical transition electron microscopy (TEM) images of  $\text{Pt}_{66}\text{Ru}_{34}$  nanocatalysts are shown in Fig. 1a, indicating a uniform dispersion. As shown in Fig. 1b, the statistical analysis based on TEM images of  $\text{Pt}_{66}\text{Ru}_{34}$  nanocatalysts indicates that the nanocatalysts have uniform diameters of  $2.3 \pm 0.03$  nm. Meanwhile, the size distributions of other nanoparticles are shown in Fig. S1 (ESI†), which all indicate uniform dispersion with small sizes of less than 3 nm. *In situ* ultraviolet-visible absorbance spectroscopy (UV-vis) proves that five control groups catalyze the  $\text{H}_2$  (H) reduction of nonfluorescent resazurin (R) to the highly fluorescent product resorufin (P) at the ensemble level (Fig. S2a–e, ESI†). The absorption spectrum shows a decrease of resazurin

absorption at 601 nm and an increase of resorufin absorption at 571 nm over time, indicating the persistence of the reduction reaction. The evolution of the absorbance of the five control groups at 601 nm and 571 nm over time is shown in Fig. 1c and d. Moreover, unchanged absorbance can be observed from the UV-vis tests performed in the absence of either  $\text{H}_2$  or nanoparticles, demonstrating a reaction process with reductive  $\text{H}_2$  catalyzed by metallic nanoparticles (Fig. S2f–k, ESI†). Therefore, this shows that the apparent reaction rate is as follows:  $\text{Pt}_{66}\text{Ru}_{34} > \text{Pt}_{76}\text{Ru}_{24} > \text{Pt}_{39}\text{Ru}_{61} > \text{Pt} > \text{Ru}$ . The results demonstrate that the catalytic efficiencies of bimetallic nanocatalysts vary with different ratios, but they are all higher than those of monometallic catalysts.

Single particle experiments were conducted with a home-made flow cell (Fig. 2a). Briefly, nanocatalysts were immobilized sparsely on the surface of quartz coverslips. A  $\text{H}_2$ -saturated solution was delivered with a syringe pump with varying resazurin concentrations (ranging from 1 to 10 nM) into microfluidic channels, where the reactions occur. The resorufin product was generated on the surface of nanoparticles under excitation with a 532 nm laser, and the fluorescence signal was captured using a total internal reflection fluorescence microscope (TIRFM) equipped with an electron-multiplying charge-coupled device camera. The camera was operated at 100 ms per frame to record movies, in which stochastic fluorescence bursts at numerous localized spots on the glass surface were shown with each point emitting fluorescence repeatedly. Each fluorescence burst was attributed to a single reaction in which a nanoparticle catalyzed the conversion of resazurin into the fluorescent product resorufin. The dissociated product molecules in the solution cannot be detected at our image speed due to their rapid diffusion.<sup>36</sup> The movies were processed using a home-written Interactive Data Language program to obtain fluorescence burst trajectories at each location (as shown in Fig. 2b). These fluorescence trajectories revealed stochastic switching signals, with individual nanoparticle turnover trajectories characterized by two waiting times:  $\tau_{\text{off}}$  and  $\tau_{\text{on}}$ .  $\tau_{\text{off}}$  is the waiting time before each product formation and  $\tau_{\text{on}}$  is that for product desorption after its formation. The kinetic mechanism of catalytic product formation and product desorption reactions could be probed separately by resolving them. The values of  $\tau_{\text{off}}$  and  $\tau_{\text{on}}$  are stochastic, but they have statistical regularities, such as averages and distributions, which can be effectively integrated with the reaction kinetics. In a statistical sense,  $\langle \tau_{\text{off}} \rangle^{-1}$  and  $\langle \tau_{\text{on}} \rangle^{-1}$  (" $\langle \rangle$ " represents the average value) represent the average reaction rate of the product formation and product desorption, respectively.

Through separately averaging turnover trajectories of nanocatalysts such as  $\text{Pt}_{66}\text{Ru}_{34}$ ,  $\text{Pt}_{76}\text{Ru}_{24}$ ,  $\text{Pt}_{39}\text{Ru}_{61}$ , Pt and Ru, the dependency of reaction rates on the resazurin concentration for the five types of nanocatalysts can be obtained (Fig. 2c and d). It can be clearly concluded that the product formation rate  $\langle \tau_{\text{off}} \rangle^{-1}$  initially increases with the increase in resazurin concentration and then declines at higher resazurin concentrations after reaching a maximum value. The variation in  $\langle \tau_{\text{off}} \rangle^{-1}$  is attributed to the competitive adsorption reaction of

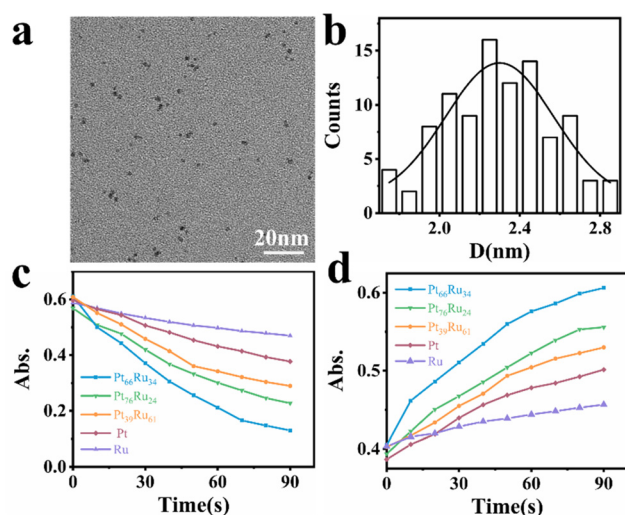


**Fig. 1** (a) TEM image of  $\text{Pt}_{66}\text{Ru}_{34}$  nanocatalysts and (b) size distribution of  $\text{Pt}_{66}\text{Ru}_{34}$  nanoparticles with an average of about  $2.3 \pm 0.03$  nm. Dependence of (c) 601 nm and (d) 571 nm absorbance on time for nanocatalysts with different ratios. All of the experiments were carried out in a saturated  $\text{H}_2$  solution with the same nanoparticle concentration and resazurin concentration.



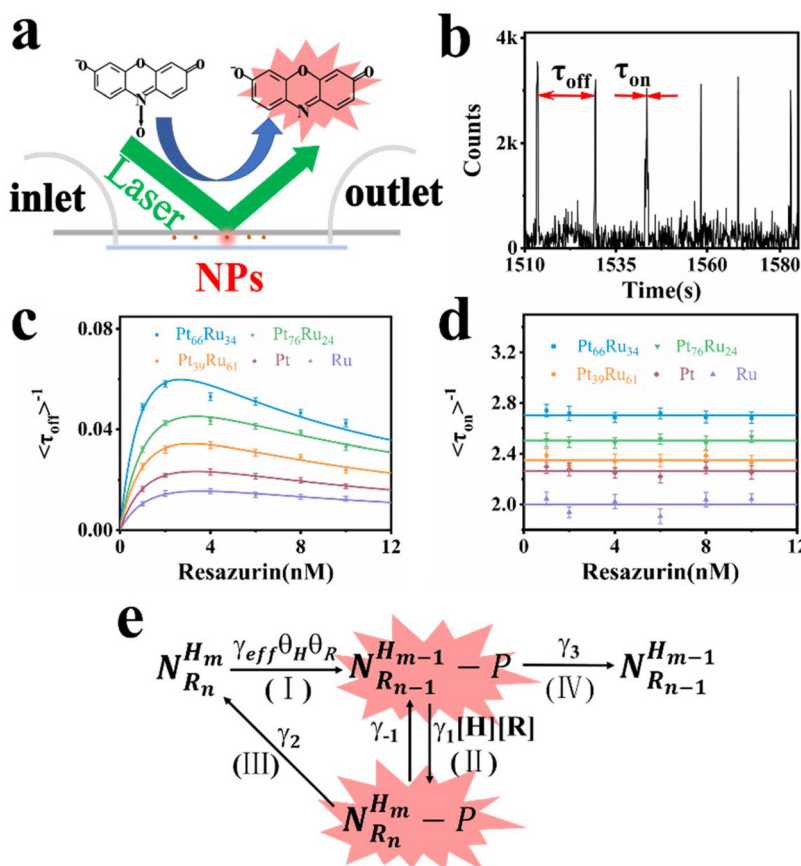


**Fig. 2** (a) The experimental setup of fluorescent catalytic reactions based on TIRFM. (b) A segment of the fluorescence turnover trajectory of a  $\text{Pt}_{66}\text{Ru}_{34}$  nanocatalyst in saturated  $\text{H}_2$  of 10 nM resazurin. (c) and (d) represent the tendency of the dependence of resazurin concentration on product formation rates and product desorption rates. Each data point is averaged over the turnover trajectories of more than 80 nanoparticles (NPs). (e) Kinetic mechanism of the reduction reaction. The meaning of each symbol is described in detail in the ESI†

the reactants: resazurin and  $\text{H}_2$  co-adsorb onto the nanoparticle surface simultaneously.<sup>37</sup> When the concentration of the substrate is very high, the other reactant will be unable to adsorb onto the nanocatalysts, leading to a decline after reaching maximum reaction rates. It is interesting that the desorption rates of the products from the control groups are independent of the resazurin concentration. It can be concluded that there are two pathways for desorption: the substrate-assisted desorption pathway and the direct product desorption pathway. When the resazurin concentration is low, the product directly desorbs. As the resazurin concentration increases, the product desorbs with the assistance of the substrate.

Based on these facts and the Langmuir-Hinshelwood mechanism, we proposed the reaction mechanism based on a bimolecular reaction model as shown in Fig. 2e. Herein, during the reaction process, the substrate and product maintain a rapid adsorption/desorption equilibrium on the surface of the nanoparticle. The dissociation process is of two types: substrate-assisted dissociation (reactions (II) and (III)) and direct desorption (reaction (IV)) of the products. Based on this mechanism, single particle kinetic analysis was performed. Single particle rate equations and some kinetic parameters

were obtained. The mathematical expressions for  $\langle\tau_{\text{off}}\rangle^{-1}$  and  $\langle\tau_{\text{on}}\rangle^{-1}$  are given by eqn (1) and (2), respectively (the detailed process is provided in the ESI†).<sup>38</sup>

$$\langle\tau_{\text{off}}\rangle^{-1} = \frac{\gamma_{\text{eff}}\alpha_{\text{H}}[\text{H}]\alpha_{\text{R}}[\text{R}]}{(1 + \alpha_{\text{H}}[\text{H}] + \alpha_{\text{R}}[\text{R}])^2} \quad (1)$$

$$\langle\tau_{\text{on}}\rangle^{-1} = \frac{\gamma_2 G[\text{R}] + \gamma_3}{1 + G[\text{R}]} \quad (2)$$

where  $\gamma_{\text{eff}}$  represents the effective catalytic rate constant of a single nanoparticle, and  $\alpha_{\text{H}}$  and  $\alpha_{\text{R}}$  are the adsorption equilibrium constants of  $\text{H}_2$  and resazurin, respectively.  $[\text{H}]$  and  $[\text{R}]$  are the concentrations of  $\text{H}_2$  and resazurin, respectively.  $\gamma_2$  and  $\gamma_3$  are the rate constants of the two desorption processes of the product,  $\gamma_1$  and  $\gamma_{-1}$  represent the reaction rate constant of reversible reaction (II), and  $G = (\gamma_1[\text{H}]/(\gamma_{-1} + \gamma_2))$  is a parameter related to  $\gamma_1$ ,  $\gamma_{-1}$  and  $\gamma_2$ .<sup>29,39</sup>

As predicted by eqn (1), the forward reaction rates  $\langle\tau_{\text{off}}\rangle^{-1}$  of the five control groups exhibit an initial increase followed by a decrease with an increase in resazurin concentration, as shown in Fig. 2c. However, the five control groups show differences in reaction rates, with the catalytic rate  $\text{Pt}_{66}\text{Ru}_{34} >$



$\text{Pt}_{76}\text{Ru}_{24} > \text{Pt}_{39}\text{Ru}_{61} > \text{Pt} > \text{Ru}$  at any concentration, which is consistent with the UV-vis data. Eqn (1) and (2) are used to fit the experimental data, and the kinetic parameters for product generation and dissociation are obtained. The parameters of the data curves fitted with equations are listed in Table 1. The results indicate that bimetallic catalysts exhibit higher rate and adsorption constants, which demonstrates that they have stronger substrate adsorption ability and higher activity. The desorption rate of the product ( $\langle\tau_{\text{on}}\rangle^{-1}$ ), as shown in Fig. 2d, is independent of the substrate concentration. However, nanocatalysts of different metal element ratios show varying desorption rates, which are consistent with the trend obtained from  $\langle\tau_{\text{off}}\rangle^{-1}$ . Based on the properties of the function in eqn (2), it can be inferred that if  $\gamma_1 \gg 0$ , then  $\gamma_2$  can be obtained from eqn (2). If  $\gamma_1 \approx 0$ , then  $\gamma_2 = \gamma_3$  can be derived from eqn (2), resulting in  $\gamma_2$  for the five control groups. Although it cannot be confirmed which of these two assumptions is correct,  $\gamma_2$  could still be obtained, as listed in Table 1. Based on these facts, bimetallic catalysts exhibit stronger catalytic activity compared to monometallic catalysts. Additionally, the catalytic activities of bimetallic catalysts vary with different ratios of metal elements. The catalytic efficiency of catalysts could be changed by adjusting the ratios of metal elements.

Furthermore, static activity was also evaluated, which represents the static heterogeneity of rates among individual nanoparticles. The probability density function of the off-time is used to evaluate the static activity of the product generation, with the following equation (see the ESI†):

$$f_{\text{off}}(\tau) = \gamma_{\text{app}} \exp(-\gamma_{\text{app}}\tau) \quad (3)$$

where  $\gamma_{\text{app}}$  is the apparent rate constant for the formation of a product on the surface of a nanoparticle. The typical distribution of  $\tau_{\text{off}}$  from a fluorescence turnover trajectory of a single  $\text{Pt}_{66}\text{Ru}_{34}$  nanoparticle is shown in Fig. 3a. The decay constant of the distribution is the apparent rate constant ( $\gamma_{\text{app}}$ ) shown in eqn (3). By analyzing the  $\tau_{\text{off}}$  distribution of multiple turnover trajectories of  $\text{Pt}_{66}\text{Ru}_{34}$ , the values of many  $\gamma_{\text{app}}$  were obtained. Then, the Gaussian distribution was used to calculate the distribution of  $\gamma_{\text{app}}$ , and the center value obtained by Gaussian fitting represented the  $\gamma_{\text{app}}$  value of  $\text{Pt}_{66}\text{Ru}_{34}$  (Fig. 3b). In the same manner, we obtained the  $\gamma_{\text{app}}$  values of the four control groups, see Fig. S3 (ESI†). The center values of the Gaussian distribution also exhibit a similar trend to the reaction rates (Fig. 3c orange solid line). Moreover, the  $\gamma_{\text{app}}$  dis-

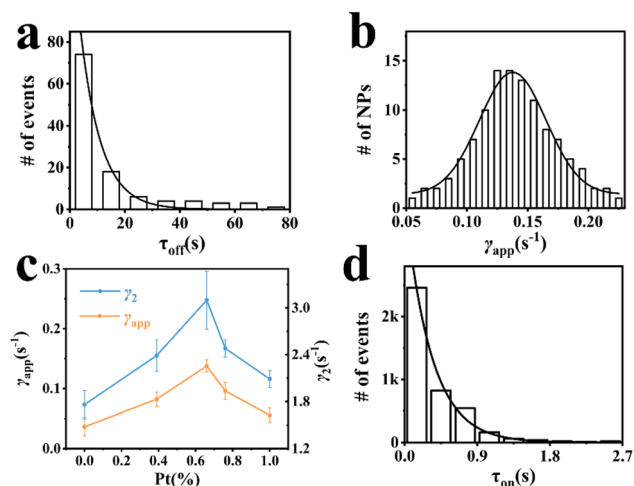


**Fig. 3** (a) Distributions of  $\tau_{\text{off}}$  from a single trajectory of a  $\text{Pt}_{66}\text{Ru}_{34}$  nanoparticle at 10 nM resazurin; the solid line is a single exponential fit with the decay constant  $\gamma_{\text{app}} = 0.13 \pm 0.012 \text{ s}^{-1}$ . (b) Distribution of  $\gamma_{\text{app}}$  of  $\text{Pt}_{66}\text{Ru}_{34}$  nanocatalysts at 10 nM resazurin; the solid line is the Gaussian fit. (c) Dependences of  $\gamma_{\text{app}}$  (orange) and  $\gamma_2$  (blue) on the percentage of Pt. (d) Distributions of  $\tau_{\text{on}}$  from over 100 trajectories of  $\text{Pt}_{66}\text{Ru}_{34}$  nanocatalysts at 10 nM resazurin; the solid line is a single exponential fit. All experiments are conducted in a  $\text{H}_2$ -saturated solution of 10 nM resazurin.

tributions of the five control groups are broad, indicating significant activity heterogeneity among individual nanoparticles. We further quantify the heterogeneity of activity using the full-width at half-maximum (FWHM), as shown in Table 2. The results indicate that the heterogeneity of activity does not show a correlation with the reaction rate, but it is evident that the FWHM of bimetallic nanocatalysts is much larger than that of monometallic nanocatalysts. Therefore, at the single particle level, it could be concluded that individual bimetallic nanoparticles with different ratios of metal elements exhibit different catalytic activities.<sup>42</sup>

For the product desorption process, when the substrate resazurin concentration is high enough, the probability density function can be simplified as follows (see the ESI†):

$$f_{\text{on}}(\tau) = \gamma_2 \exp(-\gamma_2\tau) \quad (4)$$

It is a single exponential function with the product desorption rate constant  $\gamma_2$  acting as the decay constant. We employed our

**Table 1** Kinetic parameters obtained from the fittings of eqn (1) and (2)<sup>a</sup>

	$\gamma_{\text{eff}} (\text{s}^{-1})$	$\alpha_{\text{H}} (\text{mM}^{-1})$	$\alpha_{\text{R}} (\text{nM}^{-1})$	$\gamma_2 (\text{s}^{-1})$
$\text{Pt}_{66}\text{Ru}_{34}$	$0.58 \pm 0.03$	$0.89 \pm 0.08$	$0.64 \pm 0.03$	$2.70 \pm 0.10$
$\text{Pt}_{76}\text{Ru}_{24}$	$0.52 \pm 0.03$	$0.65 \pm 0.04$	$0.45 \pm 0.01$	$2.50 \pm 0.09$
$\text{Pt}_{39}\text{Ru}_{61}$	$0.44 \pm 0.04$	$0.56 \pm 0.04$	$0.46 \pm 0.01$	$2.35 \pm 0.07$
Pt	$0.40 \pm 0.01$	$0.20 \pm 0.01$	$0.38 \pm 0.03$	$2.26 \pm 0.04$
Ru	$0.30 \pm 0.03$	$0.33 \pm 0.01$	$0.35 \pm 0.01$	$1.99 \pm 0.03$

<sup>a</sup> The values of the kinetic parameters are the average of many nanoparticles (>100).  $\gamma_2$  is obtained by fitting eqn (2).<sup>40,41</sup>

**Table 2** Fitting results for static and dynamic heterogeneities of nanoparticles<sup>a</sup>

	$x_c (\text{s}^{-1})$	FWHM	$\gamma_2 (\text{s}^{-1})$	$T_{\text{flu off}} (\text{s})$	$T_{\text{flu on}} (\text{s})$
$\text{Pt}_{66}\text{Ru}_{34}$	0.137	$0.065 \pm 0.004$	$3.09 \pm 0.18$	$33 \pm 2$	$36 \pm 2$
$\text{Pt}_{76}\text{Ru}_{24}$	0.096	$0.073 \pm 0.007$	$2.48 \pm 0.20$	$45 \pm 4$	$48 \pm 5$
$\text{Pt}_{39}\text{Ru}_{61}$	0.082	$0.072 \pm 0.005$	$2.39 \pm 0.14$	$64 \pm 8$	$60 \pm 8$
Pt	0.056	$0.036 \pm 0.004$	$2.08 \pm 0.11$	$97 \pm 16$	$94 \pm 15$
Ru	0.036	$0.028 \pm 0.005$	$1.75 \pm 0.11$	$136 \pm 31$	$128 \pm 28$

<sup>a</sup>  $\gamma_2$  is obtained by fitting the probability density function using eqn (4).<sup>40,41</sup>





previous method to calculate  $\tau_{\text{on}}$  for multiple turnover trajectories, yielding the fitted parameter  $\gamma_2$  (Fig. 3d and S4, ESI†). Moreover, the  $\gamma_2$  in Fig. 3c for the blue solid line exhibits a trend similar to  $\gamma_{\text{app}}$ . Therefore, the relationship between metal ratios and reaction rates for the five control groups at the single particle level is demonstrated, which enhances the understanding of bimetallic catalysts. The  $\gamma_2$  values (in Table 2) exhibit the same trend as the data shown in Table 1 obtained from the concentration-titration fitting. Therefore, this proves that the previous assumption is reasonable.

There are differences in static catalytic activities among nanocatalysts, so it is necessary to study the variability of activity in an individual nanoparticle over time, *i.e.*, the fluctuations of reaction rates. The variation in reaction rates over time for an individual nanoparticle is referred to as dynamic disorder in chemical kinetics.<sup>43</sup> This fluctuation timescale, which corresponds to the timescale of underlying surface restructuring dynamics, can be measured using autocorrelation analysis of single-turnover waiting times,  $\tau_{\text{off}}$  and  $\tau_{\text{on}}$ .<sup>44,45</sup> At high substrate concentrations, the reaction rate limitations for the off-time and on-time are denoted by  $\gamma_{\text{eff}}$  and  $\gamma_2$ , respectively. We use covariance to describe the dynamic variation of activity over time for a nanoparticle. The mathematical expression is as follows:<sup>46–48</sup>

$$C(m) = \frac{n \sum_i \tau_i \tau_{i+m} - \left( \sum_i \tau_i \right)^2}{n \sum_i \tau_i^2 - \left( \sum_i \tau_i \right)^2} = \frac{\langle \Delta\tau(0) \Delta\tau(m) \rangle}{\langle \Delta\tau^2 \rangle} \quad (5)$$

where  $i$  is an index number for a total of  $n + m$  turnovers in a trajectory;  $t_i$  is the experimentally determined on-time (or off-time); and  $m$  is the separation between the pairs of on-times (or off-times). In fact,  $C(m)$  is the autocorrelation function of the on-times or off-times (the second term of eqn (5)). In the absence of dynamic disorder,  $C(0) = 1$  and  $C(m) = 0$  ( $m > 0$ ). In the presence of dynamic disorder,  $C(m)$  is a decay function.

The insets in Fig. 4a and b depict the autocorrelation functions of the off-time and on-time of Pt<sub>66</sub>Ru<sub>34</sub> nanocatalysts, respectively, both exhibiting exponential decay, indicating dynamic activity fluctuations during product formation and desorption processes. The autocorrelation functions of the other four control groups are plotted in the insets of Fig. S5 and S6 (ESI†), and their exponential decay functions similarly indicate dynamic activity fluctuations. The decay constants of Pt<sub>66</sub>Ru<sub>34</sub> nanocatalysts are  $m_{\text{off}} = 1.50 \pm 0.32$  and  $m_{\text{on}} = 1.91 \pm 0.27$ , respectively. The average turnover time of the trajectory is denoted as 17.2 s. Therefore, we convert the turnover exponent  $m$  of the reaction process into the turnover reaction time, fitted as Fig. 4a and b, respectively. The fitted fluctuation correlation times  $\tau_{\text{off}}$  and  $\tau_{\text{on}}$  of the reactions are  $26 \pm 3$  s and  $33 \pm 2$  s, respectively. The fitted curves of the autocorrelation functions of the off-time and the on-time for the other four control groups are shown in Fig. S5 and S6 (ESI†). These two fluctuation times represent the timescales of fluctuations in  $\gamma_{\text{eff}}$  and  $\gamma_2$ , which are rate-limiting in the  $\tau_{\text{off}}$  and  $\tau_{\text{on}}$  reactions at high

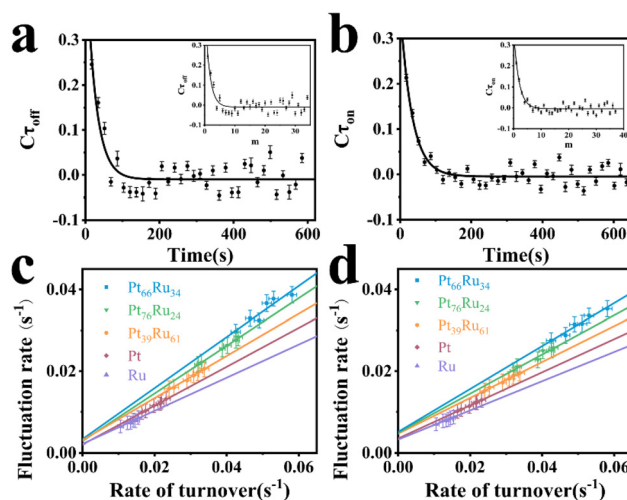


**Fig. 4** Autocorrelation function  $C\tau_{\text{off}}(t)$  (a) and  $C\tau_{\text{on}}(t)$  (b) of the reaction time  $\tau$  from turnover trajectories of Pt<sub>66</sub>Ru<sub>34</sub> nanocatalysts. Inset: autocorrelation function of the  $\tau_{\text{off}}$  (a) and  $\tau_{\text{on}}$  (b) from the turnover trajectory of a single Pt<sub>66</sub>Ru<sub>34</sub> nanoparticle; the solid line is a single exponential fit. Autocorrelation function  $C\tau_{\text{off}}(t)$  (a) and  $C\tau_{\text{on}}(t)$  (b) of the reaction time  $\tau$  from turnover trajectories of Pt<sub>66</sub>Ru<sub>34</sub> nanocatalysts. The x-axis was converted from the turnover index  $m$  to real time using the average turnover time of each nanoparticle. The solid line is a single exponential fit. Dependence of the activity fluctuation rates of (c)  $\tau_{\text{off}}$  and (d)  $\tau_{\text{on}}$  on the reaction rates. All experiments are conducted in a H<sub>2</sub>-saturated solution of 10 nM resazurin.

resazurin concentrations. The dynamic activity fluctuation was attributed to the dynamic surface restructuring on the individual nanoparticle surface. During catalysis, changes in adsorbate-surface interactions can induce dynamic surface restructuring, with kinetic disturbances due to the different activities of different surface structures.<sup>49,50</sup> For the nanocatalysts here, dynamic surface restructuring can cause dynamic activity fluctuation by changing the rate constants ( $\gamma_{\text{eff}}$  or  $\gamma_2$ ) at each catalytic site. So, the rate of dynamic activity fluctuation (reciprocal of fluctuation correlation times) should increase with the reaction rate (rate of turnover). To support this attribution, we need to determine the dependence of the dynamic activity fluctuation rate on the reaction rate. We counted the decay constants of a large amount of Pt<sub>66</sub>Ru<sub>34</sub> nanoparticles to obtain the average fluctuation correlation times  $T_{\text{flu,off}}$  (and  $T_{\text{flu,on}}$ ), listed in Table 2. The average fluctuation correlation time of the other four control groups is also listed in Table 2. The relationship between the reaction rates and the activity fluctuation rates is illustrated in Fig. 4c and d. We found a positive correlation between the reaction rates and the activity fluctuation of an individual nanoparticle, suggesting that reactions indeed induce surface restructuring of nanocatalysts. Extrapolating activity fluctuation rates to zero, the intercepts provide approximate rates of spontaneous surface restructuring during the  $\tau_{\text{off}}$  and  $\tau_{\text{on}}$  processes of nanocatalysts.<sup>29,51</sup> The timescales of spontaneous surface restructuring ( $>200$  s) are longer than that of the catalysis-induced surface restructuring process, indicating that surface restructuring of nanocatalysts



is predominantly induced under catalytic conditions. In addition, the slope of bimetallic nanocatalysts is higher than that of monometallic nanocatalysts, showing a greater rate of fluctuation in the dynamic activity of bimetallic nanocatalysts and higher activity.

Based on the above data obtained from the single-molecule fluorescence technique, the PtRu bimetallic catalysts exhibit enhanced catalytic performance compared to the monometallic Pt or Ru samples. The reason for this is inferred to be the accelerated catalytic kinetics arising from the regulated electron structure of active sites or the synergistic effect of diverse active sites. On the one hand, the electron structure of active sites can be tuned by the formation of alloys, which facilitates the sorption of reactive species and thus improves the catalytic kinetics.<sup>52</sup> On the other hand, considering the presence of adjacent Pt and Ru sites, the synergistic effect, which is adsorbing different reactants on diverse active sites, may also be the reason for the enhanced activity of PtRu bimetallic catalysts.<sup>53</sup>

## Conclusions

From a single particle perspective, we investigated the catalytic behaviors of bimetallic and monometallic catalysts. By studying the relationship between catalytic reaction rates and substrate concentrations, the reaction mechanisms of the five control groups all followed a competitive adsorption Langmuir–Hinshelwood model. By analyzing turnover trajectories during product formation, we discovered that bimetallic nanoparticles exhibit greater activity heterogeneity compared to monometallic nanoparticles. Autocorrelation analysis indicates dynamic fluctuations in activity during both product generation and desorption processes, with the rate of these fluctuations positively correlated with reaction rates. The high catalytic activity of the bimetallic catalyst is attributed to its high dynamic activity fluctuation rate. This work deepens understanding of the differences between bimetallic and monometallic catalysts and provides a good reference at the nanoscale for the design of metallic catalysts.

## Author contributions

Bowei Zhang: methodology, validation, formal analysis, investigation, data curation, writing – original draft, and visualization. Dezheng Zhang: investigation. Jinpeng Bao: investigation and supervision. Ce Han: conceptualization, supervision, and resources. Ping Song: conceptualization, supervision, and resources. Weilin Xu: conceptualization, resources, writing – review and editing, supervision, and funding acquisition.

## Data availability

The data supporting this article have been included as part of the ESI.†

## Conflicts of interest

The authors declare no competing financial interest.

## Acknowledgements

This work was supported by the National Natural Science Foundation of China (21925205, 22072145, 22372155, and 22102172).

## References

- 1 S. Ashraf, Y. Y. Liu, H. J. Wei, R. F. Shen, H. H. Zhang, X. L. Wu, S. Mehdi, T. Liu and B. J. Li, *Small*, 2023, **19**, 48.
- 2 J. L. Liu, T. R. Zhang and G. I. N. Waterhouse, *J. Mater. Chem. A*, 2020, **8**, 23142–23161.
- 3 J. G. Smith, I. Chakraborty and P. K. Jain, *Angew. Chem., Int. Ed.*, 2016, **55**, 9979–9983.
- 4 K. D. Gilroy, A. Ruditskiy, H. C. Peng, D. Qin and Y. N. Xia, *Chem. Rev.*, 2016, **116**, 10414–10472.
- 5 L. C. Liu and A. Corma, *Chem. Rev.*, 2023, **123**, 4855–4933.
- 6 S. Q. Zhu, X. P. Qin, F. Xiao, S. L. Yang, Y. Xu, Z. Tan, J. D. Li, J. W. Yan, Q. Chen, M. S. Chen and M. H. Shao, *Nat. Catal.*, 2021, **4**, 711–718.
- 7 Y. Wang, G. W. Wang, G. W. Li, B. Huang, J. Pan, Q. Liu, J. J. Han, L. Xiao, J. T. Lu and L. Zhuang, *Energy Environ. Sci.*, 2015, **8**, 177–181.
- 8 D. J. Chen and Y. Y. J. Tong, *Angew. Chem., Int. Ed.*, 2015, **54**, 9394–9398.
- 9 D. Strmcnik, M. Uchimura, C. Wang, R. Subbaraman, N. Danilovic, D. van der Vliet, A. P. Paulikas, V. R. Stamenkovic and N. M. Markovic, *Nat. Chem.*, 2013, **5**, 300–306.
- 10 L. Huang, X. P. Zhang, Q. Q. Wang, Y. J. Han, Y. X. Fang and S. J. Dong, *J. Am. Chem. Soc.*, 2018, **140**, 1142–1147.
- 11 H. S. Liu, C. J. Song, L. Zhang, J. J. Zhang, H. J. Wang and D. P. Wilkinson, *J. Power Sources*, 2006, **155**, 95–110.
- 12 J. M. Wang, B. X. Zhang, X. Z. Zheng, X. R. Liu, W. Guo, Z. X. Luo, Y. F. Liu, M. X. Gao, J. Chen, Z. B. Zhuang, H. G. Pan and W. P. Sun, *Nano Res.*, 2024, **17**, 6147–6156.
- 13 S. Yin, K. N. Zong, L. S. Ban, H. M. Yin, X. Z. Liu and Y. Ding, *Inorg. Chem. Front.*, 2024, **11**, 3633–3642.
- 14 T. Iwasita, H. Hoster, A. John-Anacker, W. F. Lin and W. Vielstich, *Langmuir*, 2000, **16**, 522–529.
- 15 E. Antolini and F. Cardellini, *J. Alloys Compd.*, 2001, **315**, 118–122.
- 16 H. N. Dinh, X. M. Ren, F. H. Garzon, P. Zelenay and S. Gottesfeld, *J. Electroanal. Chem.*, 2000, **491**, 222–233.
- 17 S. L. Gojkovic, T. R. Vidakovic and D. R. Durovic, *Electrochim. Acta*, 2003, **48**, 3607–3614.
- 18 Y. C. Wei, X. X. Wu, Y. L. Zhao, L. Wang, Z. Zhao, X. T. Huang, J. Liu and J. M. Li, *Appl. Catal., B*, 2018, **236**, 445–457.



- 19 J. K. Norskov, F. Abild-Pedersen, F. Studt and T. Bligaard, *Proc. Natl. Acad. Sci. U. S. A.*, 2011, **108**, 937–943.
- 20 W. T. Yu, M. D. Porosoff and J. G. G. Chen, *Chem. Rev.*, 2012, **112**, 5780–5817.
- 21 X. G. Guo, G. Z. Fang, G. Li, H. Ma, H. J. Fan, L. Yu, C. Ma, X. Wu, D. H. Deng, M. M. Wei, D. L. Tan, R. Si, S. Zhang, J. Q. Li, L. T. Sun, Z. C. Tang, X. L. Pan and X. H. Bao, *Science*, 2014, **344**, 616–619.
- 22 D. Kim, J. Resasco, Y. Yu, A. M. Asiri and P. D. Yang, *Nat. Commun.*, 2014, **5**, 8.
- 23 P. Chen, X. C. Zhou, N. M. Andoy, K. S. Han, E. Choudhary, N. M. Zou, G. Q. Chen and H. Shen, *Chem. Soc. Rev.*, 2014, **43**, 1107–1117.
- 24 P. Chen, X. C. Zhou, H. Shen, N. M. Andoy, E. Choudhary, K. S. Han, G. K. Liu and W. L. Meng, *Chem. Soc. Rev.*, 2010, **39**, 4560–4570.
- 25 K. P. F. Janssen, G. De Cremer, R. K. Neely, A. V. Kubarev, J. Van Loon, J. A. Martens, D. E. De Vos, M. B. J. Roeffaers and J. Hofkens, *Chem. Soc. Rev.*, 2014, **43**, 990–1006.
- 26 G. De Cremer, B. F. Sels, D. E. De Vos, J. Hofkens and M. B. J. Roeffaers, *Chem. Soc. Rev.*, 2010, **39**, 4703–4717.
- 27 J. Cao, D. Z. Zhang and W. L. Xu, *Curr. Opin. Electrochem.*, 2023, **41**, 8.
- 28 R. Ye, X. C. Sun, X. W. Mao, F. S. Alfonso, S. Baral, C. M. Liu, G. W. Coates and P. Chen, *Nat. Chem.*, 2024, **16**, 10.
- 29 W. L. Xu, J. S. Kong, Y. T. E. Yeh and P. Chen, *Nat. Mater.*, 2008, **7**, 992–996.
- 30 X. D. Liu, X. Ge, J. Cao, Y. Xiao, Y. Wang, W. Zhang, P. Song and W. L. Xu, *Proc. Natl. Acad. Sci. U. S. A.*, 2022, **119**, 7.
- 31 B. Dong, Y. C. Pei, F. Zhao, T. W. Goh, Z. Y. Qi, C. X. Xiao, K. C. Chen, W. Y. Huang and N. Fang, *Nat. Catal.*, 2018, **1**, 135–140.
- 32 R. Hao, Y. S. Fan, M. D. Howard, J. C. Vaughan and B. Zhang, *Proc. Natl. Acad. Sci. U. S. A.*, 2018, **115**, 5878–5883.
- 33 G. Q. Chen, N. M. Zou, B. Chen, J. B. Sambur, E. Choudhary and P. Chen, *ACS Cent. Sci.*, 2017, **3**, 1189–1197.
- 34 X. D. Qu, B. L. Zhao, W. S. Zhang, J. H. Zou, Z. X. Wang, Y. W. Zhang and L. Niu, *J. Phys. Chem. Lett.*, 2022, **13**, 830–837.
- 35 Y. Shimazaki, Y. Kobayashi, S. Yamada, T. Miwa and M. Konno, *J. Colloid Interface Sci.*, 2005, **292**, 122–126.
- 36 X. C. Zhou, N. M. Andoy, G. K. Liu, E. Choudhary, K. S. Han, H. Shen and P. Chen, *Nat. Nanotechnol.*, 2012, **7**, 237–241.
- 37 G. A. Somorjai, *J. Phys. Chem. B*, 2000, **104**, 2969–2979.
- 38 W. L. Xu, J. S. Kong and P. Chen, *J. Phys. Chem. C*, 2009, **113**, 2393–2404.
- 39 T. Chen, Y. W. Zhang and W. L. Xu, *Phys. Chem. Chem. Phys.*, 2016, **18**, 22494–22502.
- 40 P. Chen, W. L. Xu, X. C. Zhou, D. Panda and A. Kalininskiy, *Chem. Phys. Lett.*, 2009, **470**, 151–157.
- 41 Y. Xiao, J. Hong, X. Wang, T. Chen, T. Hyeon and W. L. Xu, *J. Am. Chem. Soc.*, 2020, **142**, 13201–13209.
- 42 S. Alayoglu, A. U. Nilekar, M. Mavrikakis and B. Eichhorn, *Nat. Mater.*, 2008, **7**, 333–338.
- 43 W. L. Xu, J. S. Kong and P. Chen, *Phys. Chem. Chem. Phys.*, 2009, **11**, 2767–2778.
- 44 S. L. Yang and J. S. Cao, *J. Phys. Chem. B*, 2001, **105**, 6536–6549.
- 45 S. L. Yang and J. S. Cao, *J. Chem. Phys.*, 2002, **117**, 10996–11009.
- 46 H. P. Lu, L. Y. Xun and X. S. Xie, *Science*, 1998, **282**, 1877–1882.
- 47 S. C. Kou, B. J. Cherayil, W. Min, B. P. English and X. S. Xie, *J. Phys. Chem. B*, 2005, **109**, 19068–19081.
- 48 M. J. Schnitzer and S. M. Block, *Nature*, 1997, **388**, 386–390.
- 49 R. Imbihl and G. Ertl, *Chem. Rev.*, 1995, **95**, 697–733.
- 50 D. A. King, *Surf. Rev. Lett.*, 1994, **01**, 435–442.
- 51 P. Chen, W. L. Xu, X. C. Zhou, D. Panda and A. Kalininskiy, *Chem. Phys. Lett.*, 2009, **470**, 151–157.
- 52 K. W. Park, J. H. Choi, B. K. Kwon, S. A. Lee, Y. E. Sung, H. Y. Ha, S. A. Hong, H. Kim and A. Wieckowski, *J. Phys. Chem. B*, 2002, **106**, 1869–1877.
- 53 L. X. Huo, C. Q. Jin, J. L. Tang, X. H. Xu, K. Jiang, L. Y. Shang, Y. W. Li, J. Z. Zhang, L. Q. Zhu, J. H. Chu and Z. G. Hu, *ACS Appl. Energy Mater.*, 2022, **5**, 15136–15145.

